NANO LETTERS

pubs.acs.org/NanoLett

Letter

Ligand-Assisted Reconstruction of Colloidal Quantum Dots Decreases Trap State Density

Bin Sun, Maral Vafaie, Larissa Levina, Mingyang Wei, Yitong Dong, Yajun Gao, Hao Ting Kung, Margherita Biondi, Andrew H. Proppe, Bin Chen, Min-Jae Choi, Laxmi Kishore Sagar, Oleksandr Voznyy, Shana O. Kelley, Frédéric Laquai, Zheng-Hong Lu, Sjoerd Hoogland, F. Pelayo García de Arquer, and Edward H. Sargent*

Cite This: https://dx.doi.org/10.1021/acs.nanolett.0c00638

Read Online

ABSTRACT: Increasing the power conversion efficiency (PCE) of colloidal quantum dot (CQD) solar cells has relied on improving the passivation of CQD surfaces, enhancing CQD coupling and charge transport, and advancing device architecture. The presence of hydroxyl groups on the nanoparticle surface, as well as dimers—fusion between CQDs—has been found to be the major source of trap states, detrimental to optoelectronic properties and device performance. Here, we introduce a CQD reconstruction step that decreases surface hydroxyl groups and dimers simultaneously. We explored the dynamic interaction of charge carriers between band-edge states and trap states in CQDs using time-resolved spectroscopy, showing that trap to ground-state recombination occurs mainly from surface defects in coupled CQD solids passivated using simple metal halides. Using CQD reconstruction, we demonstrate a 60% reduction in trap density and a 25% improvement in charge diffusion length. These translate into a PCE of 12.5% compared to 10.9% for control CQDs.

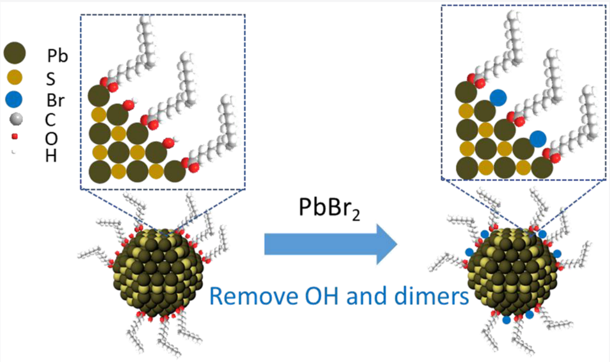

KEYWORDS: *Quantum dots, surface defects, trap states, dimers, photovoltaics*

Colloidal quantum dots (CQDs) have attracted interest in solar cell applications in view of their widely tunable band gap and their solution processing.[1−6] Device efficiencies have been increased via improved ligand exchanges,[7,8] increased CQD homogeneity and coupling,[9] and new device architectures.[10,11] The best performance CQD solar cell has been built on a bulk heterojunction active layer—separating photoexcited electrons and holes into distinct phases, achieving a power conversion efficiency (PCE) of 13.3%.[12]

We posited that the quality of as-synthesized CQDs' polydispersity and surface defects continues to impact the density of trap states, which influences the open-circuit voltage[13,14] and also the charge-carrier recombination.[15] Lead chloride treatment has been reported to improve the monodispersity of PbS CQD ensembles.[16] However, the application of $PbCl_2$-treated CQDs in optoelectronic devices has not been reported; this may be due to the reduced carrier transport caused by the $PbCl_x$ shell.[17−19] Recently, epitaxial dimers—pairs of CQDs fused together with an epitaxially registered crystal structure at their interface—have been found to be major sources of trap states in thiol-based ligand-passivated PbS CQD solids.[20]

Additionally, Zherebetskyy et al. reported that hydroxyl (OH) groups stay on PbS(111) facets during synthesis when using PbO as a precursor.[21] Halide anions (Cl^-, Br^-, and I^-) and molecular halide passivation have been reported as an effective route to reduce the density of dangling bonds and trap states by replacing organic long ligands, leading to improved PCE.[4,7,17,22,23] Unfortunately, OH groups are not readily removed during the ligand exchange process, and they end up acting as surface trap states in CQD solids.[24] It has been previously reported that employing $PbAc_2$ and PbX_2 ($X = Cl^-$, Br^-, and I^-)[25−28] instead of PbO during the preparation of the lead oleate precursor leads to the partial removal of OH groups during synthesis.[25] However, the residual OH was enough to limit the PCE to under 11%.[25,28]

Received: February 13, 2020
Revised: March 25, 2020
Published: March 31, 2020

ACS Publications

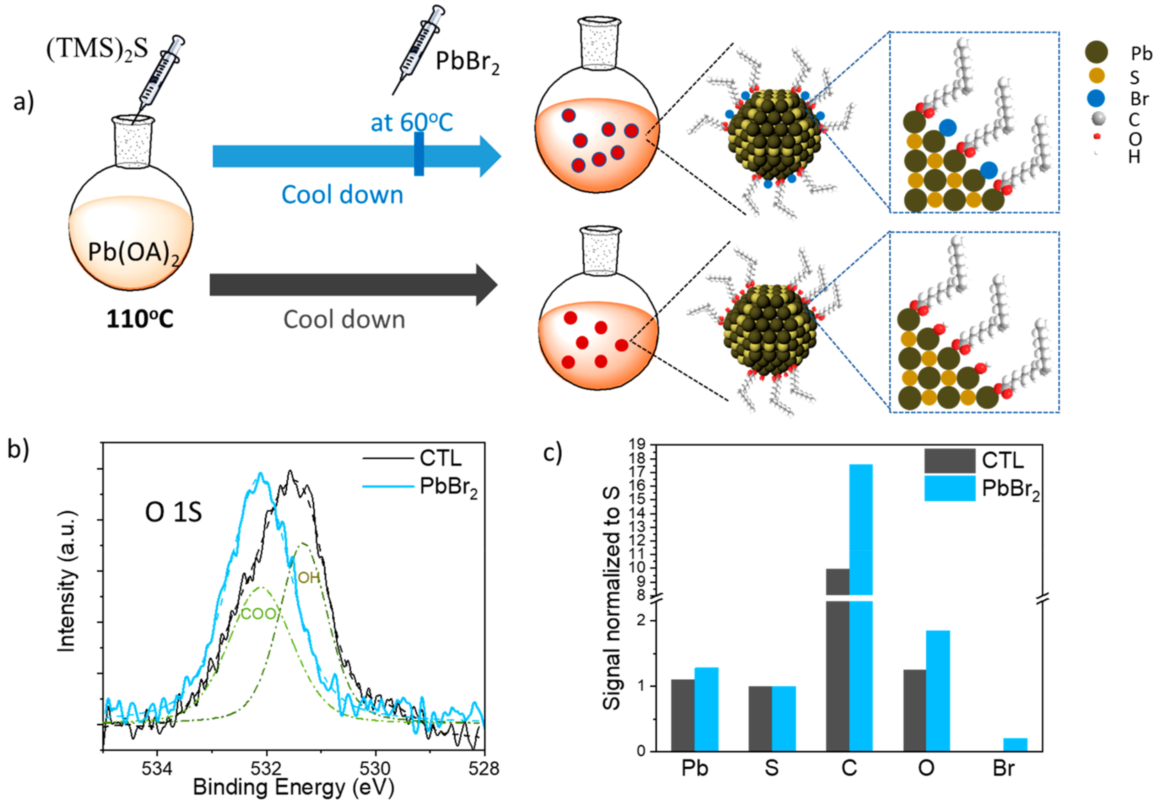

Figure 1. Improved surface passivation via $PbBr_2$ reconstruction. (a) $PbBr_2$ in-synthesis reconstruction. (b) O 1s signal from CQDs with and without $PbBr_2$ reconstruction. (c) Elemental ratios of CQDs with and without $PbBr_2$ reconstruction extracted from X-ray photoelectron spectroscopy.

Here, we report a surface reconstruction process that decreases the number of OH surface groups and dimers using halides at the cooling stage of the synthesis. At the end of synthesis, ligand digestive ripening[29] and Ostwald ripening[30] are in competition with one another by adding ligands. Ligand digestive ripening narrows CQD size distribution with the help of ligands that dissolve large particles completely—releasing monomers for the growth of the smaller sized ensembles.[31] Ostwald ripening is the inverse process, wherein small particles are dissolved.[32] By controlling these two processes, we reconstruct the CQDs, achieving improved CQD monodispersity (size dispersity 2.7%) and reduced density of OH groups on CQD surfaces. We reduce the density of trap states by 60%, mainly due to fewer surface defects, confirmed by tracking trap to ground-state recombination using time-resolved spectroscopy. The decreased surface defects also led to a longer carrier lifetime and diffusion lengths, translating into CQD solar cells exhibiting higher PCEs of 12.5% compared to 10.9% for untreated CQDs. In general, our results not only revealed the major source of trap states in metal-halide-passivated CQD solids but also provided a new path to further improve the CQD quality via a CQD reconstruction process.

■ RESULTS

We synthesized the CQDs following a modified method from Hines et al.[33] When the CQD solution was cooled to 60 °C near the end of the synthesis, $PbBr_2$ in oleylamine[34] was injected in the CQD solution (Figure 1a). The Br^- anions function as an etching agent,[35] enabling the ripening process to reconstruct CQDs and improve the size distribution.

In order to thoroughly understand how the $PbBr_2$ reconstruction affects the CQDs' surface properties, we performed X-ray photoelectron spectroscopy (XPS) analyses on the synthesized CQDs. We observed a dramatically reduced amount of OH groups and the presence of Br^- on the CQD surface following the reconstruction (Figure 1b). The CTL–PbS CQDs' XPS spectrum contains two peaks at 532.1 and 531.3 eV, corresponding to the carboxyl (COO) and OH groups, respectively, in agreement with the previously reported surface –OH groups.[21,25] In contrast, the OH signal is undetectable for the CQDs after $PbBr_2$ reconstruction ($PbBr_2$–PbS). After the O 1s peak is integrated for CTL–PbS in Figure 1b, the molar ratio of O from COO and from OH is ~1. We then extracted the elemental ratios from XPS (Figure 1c), where the signals are normalized to the S 2p peak. The O/S ratio is 1.25 for CTL–PbS (0.625 from COO and 0.625 from OH). The O/S ratio is 1.85 for $PbBr_2$–PbS, where 1.225 (1.85–0.625) is approximately the additional COO after reconstruction (~100% increased O/S ratio by replacing OH with COO). This suggests that most of the OH is replaced by COO, leading to ~200% more oleic acid ligands on PbS surfaces and better passivation. The CTL–PbS and $PbBr_2$–PbS show a Pb/S ratio of 1.1 and 1.28, respectively. The $PbBr_2$–PbS has a higher Pb/S ratio due to the existence of Br^- ($PbBr_3^-$) passivation layers.

In order to study the CQD size distribution via the reconstruction, we performed scanning transmission electron microscopy (STEM) measurements for CTL–PbS (Figure 2a) and $PbBr_2$–PbS CQDs (Figure 2b). The STEM images show highly monodispersed CQDs with a mean diameter of ~3.13 ± 0.14 nm for the CTL–PbS and ~3.14 ± 0.12 the $PbBr_2$–PbS

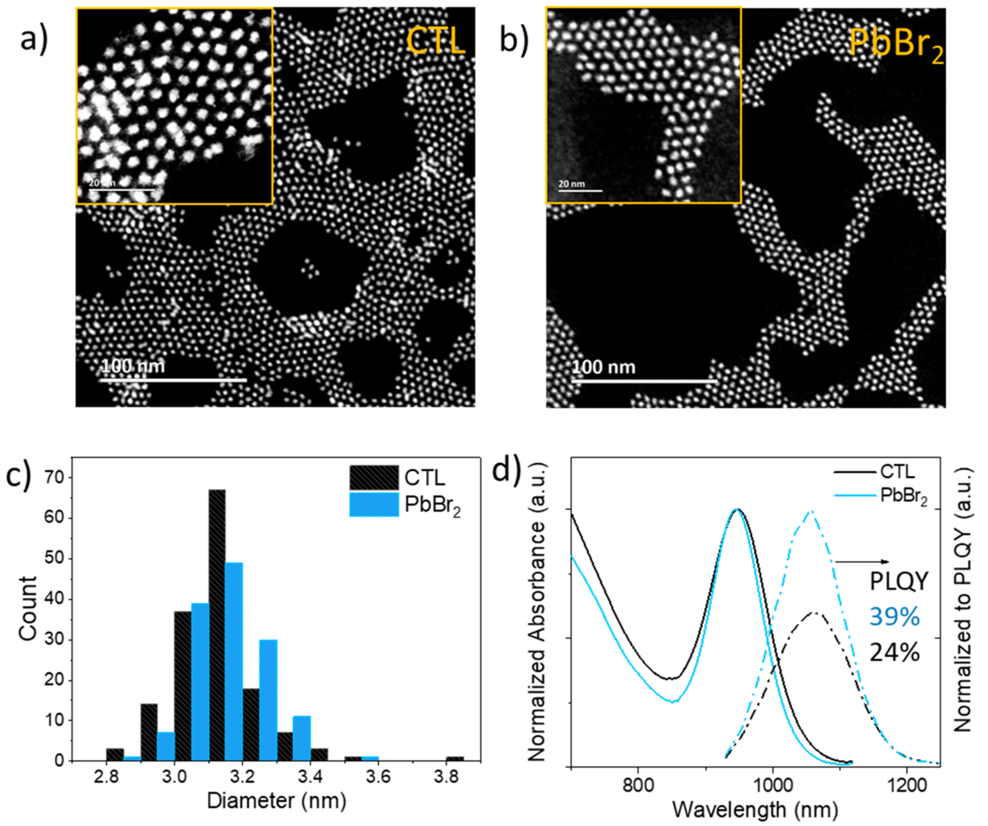

Figure 2. Reduced size distribution via $PbBr_2$ reconstruction. STEM micrograph of (a) CTL−PbS (∼20 dimers out of ∼2000 QDs from the STEM) and (b) $PbBr_2$−PbS CQDs with a zoomed-in view inset (inset scale bar, 20 nm). (c) STEM extracted particle size distribution histograms for the CTL−PbS and $PbBr_2$−PbS samples and (d) absorption and photoluminescence of CTL−PbS and $PbBr_2$−PbS CQD solution.

CQDs by analyzing ∼150 of QDs (Figure 2c; dimers are not counted). However, a higher number of dimers (the concentration of dimers is ∼1 per 100 QDs, from TEM results) can be observed in the STEM images of CTL−PbS (Figures 2a and S1), compared to the $PbBr_2$−PbS CQDs, where no dimers are observed in the STEM images. We attribute the reduced number of dimers to the digestive ripening mechanism, which causes larger nanoparticles to slowly dissolve in favor of smaller ones via etching and stabilization of the surfaces by Br^- ligands.[31]

To study the effect of the reduced OH groups and the decreased dimers, we performed absorbance (Abs) and photoluminescence (PL) measurements (Figure 2d). The half-width at half-maximum (HWHM) value of the first excitonic peak is 70 and 60 meV for CTL−PbS and $PbBr_2$−PbS, respectively (Figure S2). These values correspond to a decrease in size dispersity from 3.0% for CTL−PbS to 2.7% for $PbBr_2$−PbS CQDs,[36] which is close to the smallest value reported for PbS CQDs.[16] The $PbBr_2$ reconstruction also results in an increase of the peak-to-valley ratio from 2.9 to 4.0 and improves the PL spectrum full width at half-maximum (FWHM) value (134 meV for $PbBr_2$−PbS and 155 meV for CTL−PbS, Figure S2). These improvements are attributed to the reduction of the number of dimers following the $PbBr_2$ reconstruction, in agreement with the STEM results.

Because of the combination of improved surface passivation and monodispersity, the photoluminescence quantum yield (PLQY) of the CQDs improves from 24 to 39% for $PbBr_2$−PbS (Figure S3). This is an indicator of reduced trap density, ideal for photovoltaic applications.

Considering these promising results, we studied the optoelectronic properties of CQD solids fabricated with ligand-exchanged CQDs. We used a previously reported one-step solution-phase ligand exchange to replace the long oleic acid ligands with halides.[7] Oleic acid CQDs were ligand-exchanged from the nonpolar octane phase into the polar *N*,*N*-dimethylformamide (DMF) phase containing $PbBr_2$, PbI_2, and ammonium acetate (NH_4Ac). We performed XPS measurements (Figure S4) on exchanged CQD films and found that the organic long ligands were replaced by lead halide (Br^- and I^-) ligands.[7] A broad O 2p peak for the CTL−PbS CQD solid (Figure S4a) following ligand exchange was also observed by XPS, indicating the residual OH groups from the as-synthesized CTL−PbS CQDs; in contrast, the $PbBr_2$−PbS CQD films show a sharp O 2p peak, corresponding to carboxyl (COO) from oleic acid and acetic acid ligands. We also carried out absorption measurements on exchanged CQDs (Figure S4c). The exchanged $PbBr_2$−PbS CQDs show a better monodispersity in both DMF solution and films, indicating that the low size distribution is maintained after ligand exchange.

We employed field-effect transistor (FET) measurements to characterize the CQDs' transport properties.[8] We utilized a bottom-gate top-contact FET configuration, where 70 nm of Ti was deposited on the glass as the gate electrode, followed by 15 nm of ZrO_2 for a gate dielectric, providing a gate capacitance of 460 nF cm^{-2}. A thin 100 nm CQD film was deposited on the ZrO_2 gate dielectric, and 100 nm Au source and drain electrodes were deposited by thermal evaporation (Figure 3a). FET transfer characteristics reveal n-type

https://dx.doi.org/10.1021/acs.nanolett.0c00638
Nano Lett. XXXX, XXX, XXX−XXX

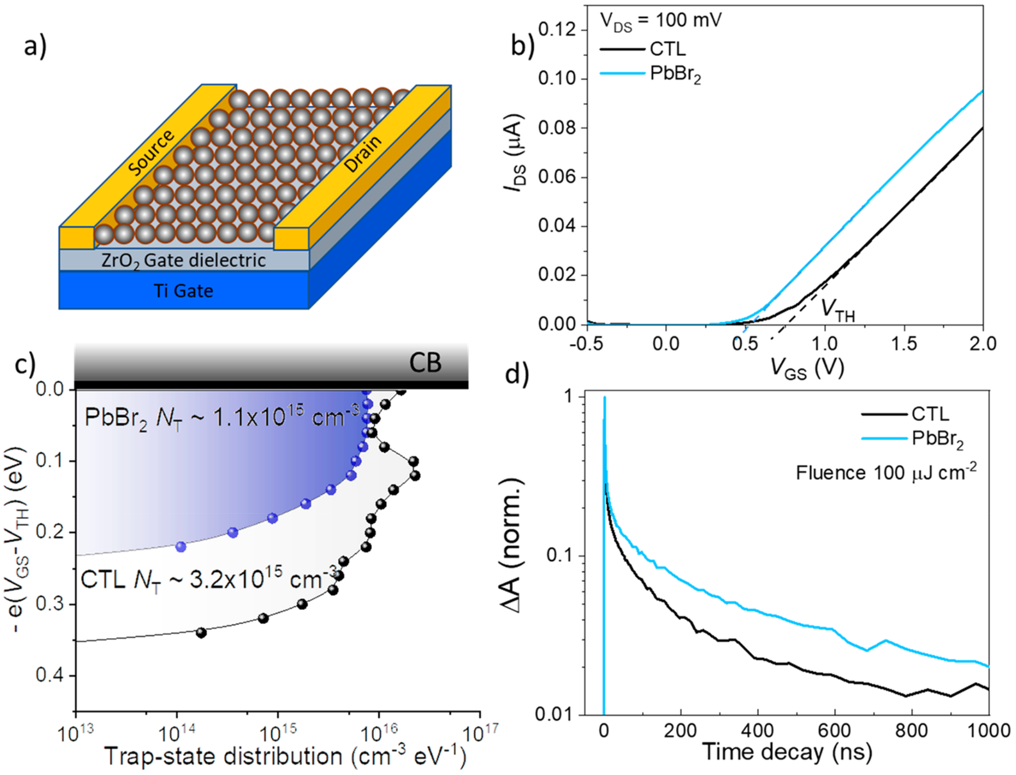

Figure 3. Improved transport properties of $PbBr_2$−PbS CQD films. (a) Bottom-gate top-contact field-effect transistor structure. (b) Transfer characteristics of exchanged PbS CQDs with/without $PbBr_2$ reconstruction. (c) Trap-state distribution (N_t) of exchanged $PbBr_2$−PbS (blue) and CTL−PbS (gray) films as calculated with eq 4 identified close to the conduction bands. (d) Kinetic traces (taken from the maximum of the band-edge exciton bleaching signal) of CTL−PbS and $PbBr_2$−PbS CQD films after ligand exchange.

transport for both CTL−PbS and $PbBr_2$−PbS CQD films (Figure 3b). We calculated carrier mobility from the slope of the drain−source current (I_{DS}) versus gate voltage (V_{GS}) according to the equation

$$I_{DS} = \mu C_i \frac{W}{L} - \left(V_{GS} - V_{TH}\right) V_{DS} \tag{1}$$

where μ is the carrier mobility in the linear regime, I_{DS} is the drain−source current, C_i is the gate dielectric layer capacitance per unit area, L and W are the channel length (50 μm) and channel width (2.5 mm), respectively, and V_{GS} and V_{TH} are the gate voltage and threshold voltage, respectively. CTL−PbS and $PbBr_2$−PbS films yielded similar electron mobility values of 0.028 ± 0.002 cm^2 V^{-1} s^{-1} and 0.029 ± 0.003 cm^2 V^{-1} s^{-1}, respectively.

We then used transient absorption (TA) measurements to ascertain the carrier lifetime.[37] TA experiments were performed on different samples with photoexcitation fluences ranging from 5 to 500 μJ cm^{-2}. Transients at the same fluence for the two different samples are shown in Figure 3d and Figure S5 (other traces can be found in Figure S6). We observe a rapid decay within the first 10 ns when using stronger pump fluences due to the increased Auger recombination.[38] After 10 ns, the signal decays at slower rates and becomes slower with increasing fluence, likely due to the trap-state filling.[39] The lifetimes extracted from these measurements are consistent with previously reported lifetimes for PbS CQD solids.[39,40] For all fluences, the lifetime of $PbBr_2$−PbS films is longer than that of CTL−PbS films, indicating longer carrier lifetimes in the $PbBr_2$−PbS films.

We extracted the lifetime from the TA results (Figure S5) and calculated the diffusion length L_d[39,41] with the following formula:

$$L_d = \sqrt{D\tau} \tag{2}$$

where D is the diffusion coefficient and τ is the carrier lifetime. D is related to carrier mobility via the Einstein relation:D =

$$D = \frac{kT\mu}{q} \tag{3}$$

where k is the Boltzmann constant, T is temperature, μ is the carrier mobility, and q is the charge of the carrier. The $PbBr_2$−PbS films have a L_d of 150 ± 5 nm, more than 25% longer than that of the CTL−PbS films (120 ± 4 nm) when the lifetime is extracted from TA data pumped by 100 ± 5 μJ cm^{-2} (Figure 3d). $PbBr_2$−PbS films always show longer L_d compared to the one of the CTL−PbS films under different fluence power, where $PbBr_2$−PbS films show longer carrier lifetime with different influence (Figure S7).

We also retrieved the density of in-gap trap states from measured transfer characteristics of FETs to confirm if the as-synthesized highly monodispersed CQDs lead to a decreased density of trap states in the exchanged CQD films,[8,42] as the gate capacitance (460 nF cm^{-2}) is large enough to shift the semiconductor active layer Fermi energy by several hundred millivolts. Varying the gate bias over a range of a few hundred millivolts allowed us to map the Fermi energy shift from the exponential increase of the drain current from V_{ON} to V_{TH} (Figures S8 and 3c) in the subthreshold regime below V_{TH}, which corresponds to transport through trap states, to obtain a trap-state distribution with following the equation:

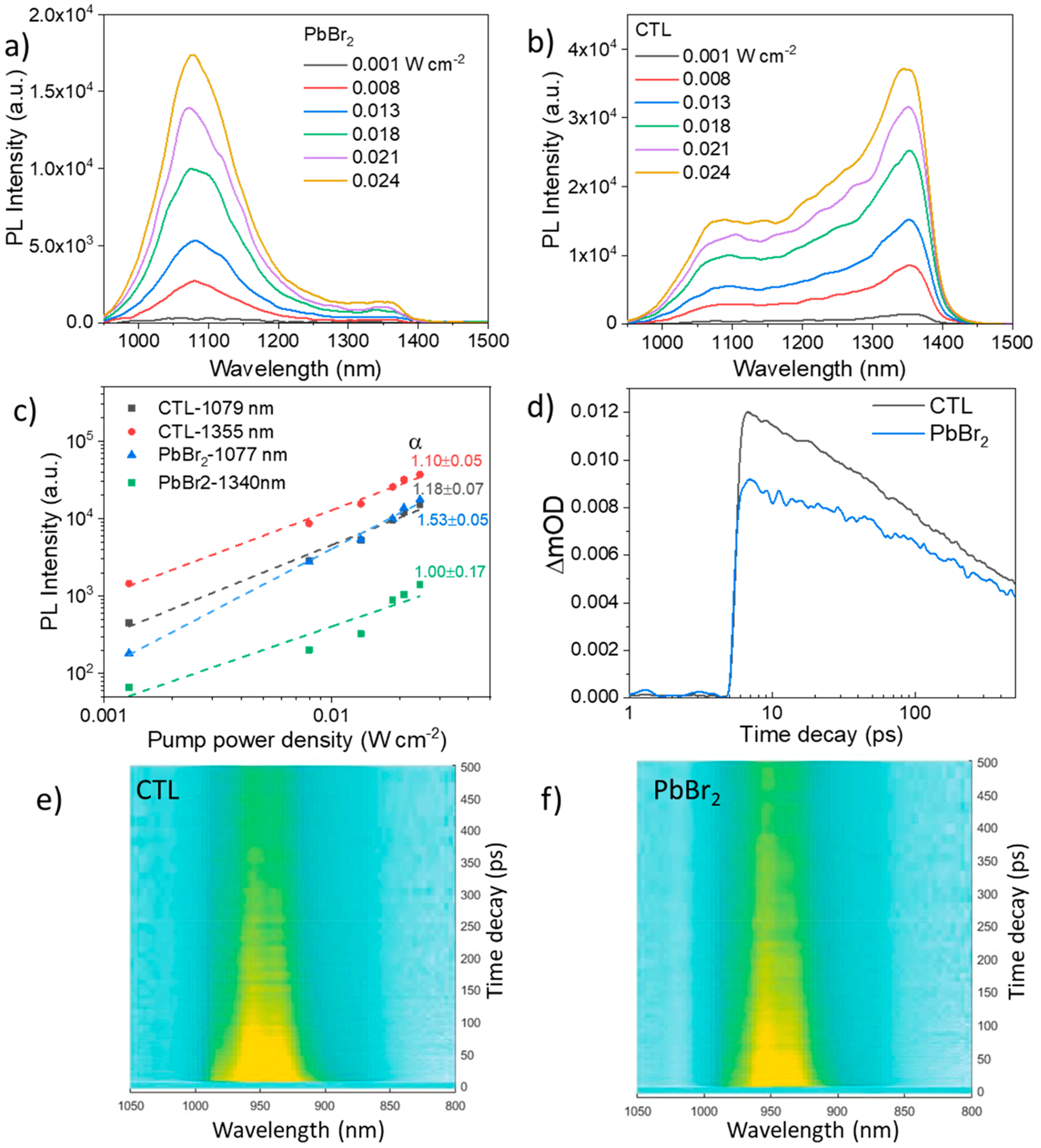

Figure 4. Decreased trap density of $PbBr_2$−PbS CQD films due to improved surface passivation. PL measurements of (a) CTL−PbS and (b) $PbBr_2$−PbS films changing excitation (at 500 nm) intensity from 0.001 to 0.024 W cm^{-2}. (c) PL intensity as a function of excitation intensities of the bands of CTL−PbS and $PbBr_2$−PbS CQD films extracted from (a) and (b). Ultrafast TA measurements: (d) band-edge bleach dynamics extracted from transient absorption of (e) CTL−PbS and (f) $PbBr_2$−PbS films pulsed at 1250 nm (0.99 eV) to excite the ground to trap state.

$$N_t = \left[\left(\frac{S\cdot e}{kT\cdot \ln(10)} - 1\right)\cdot\frac{C_i}{e}\right]^2\cdot\epsilon_0\epsilon_r^{-1} \tag{4}$$

where S is a subthreshold swing (Figure S8), the inverse of the subthreshold slope of the log drain current versus the gate voltage below V_{TH} that defines the boundary between the subthreshold and transport regime; ϵ_0 is the vacuum permittivity, and ϵ_r is the electric constant of the film, estimated to be 10.9.[43] After integrating the tail state distribution between the subthreshold and transport regime (Figure 3b) for the $PbBr_2$−PbS films, we obtained the density of tail states (N_T) (plotted in Figure 3c). The exchanged $PbBr_2$−PbS CQD film exhibits a trap density N_T of $1.5 \pm 0.3 \times 10^{15}$ cm^{-3}, lower than that of the CTL−PbS films, $5.0 \pm 0.4 \times 10^{15}$ cm^{-3}, which agrees with the above results of the longer carrier lifetime and diffusion lengths.

To study the main source of trap states in halide-passivated CQD solids, we carried out PL measurements on the films, changing the excitation intensity from 0.001 to 0.024 W cm^{-2}. CTL−PbS films show two bands of emission: the short-wavelength emission is attributed to the band-edge emission, whereas the longer wavelength peak is from the trap emission (Figure 4a). On the contrary, $PbBr_2$−PbS films show a sharp band-edge emission at 1077 nm (Figure 4b), with very weak broad trap emission at 1340 nm. This indicates a drastic reduction in the number of trap states through $PbBr_2$ reconstruction, in agreement with the FET results above. We also analyzed the recombination mechanisms using a general power law:

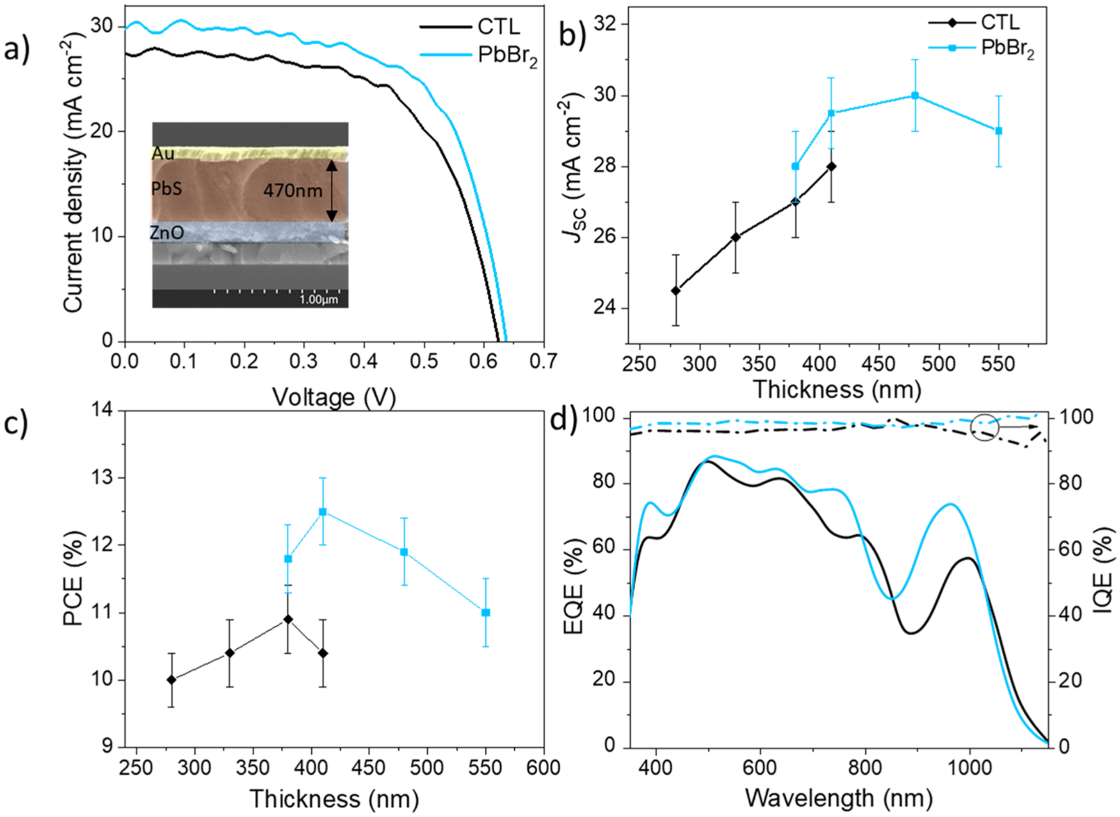

Figure 5. PV device architecture and performance. (a) Device architecture and cross-sectional scanning electron microscopy image of the best $PbBr_2$−PbS CQD film solar cell and the *J*−*V* characteristics under AM1.5G. Thickness-dependent J_{SC} (b) and PCE (c) of CTL and $PbBr_2$ PbS CQD films. (d) External quantum efficiency curves and internal quantum efficiency curves of optimal PbS CQD solar cell devices.

$$I_{PL} \propto P^{\alpha} \tag{5}$$

where I_{PL} is the PL intensity and the exponent α, depending on the radiative recombination mechanisms, is expected to be close to 1 for exciton recombination and 2 for free carrier recombination.[44]

We plotted the PL intensities of band-edge emission and trap emission for both CTL−PbS and $PbBr_2$−PbS CQD films as a function of excitation intensity and extracted the α value from the linear fitting. For CTL−PbS and $PbBr_2$−PbS films, both band-edge emission (∼1080 nm) and trap emission (∼1350 nm) intensities increased with increasing the excitation intensity with a similar α value (Figure 4c). When the averaged dimer−dimer distance (∼15 nm, calculated from the concentration of dimers, ∼1 per 100 QDs) is much smaller than the carrier diffusion length (∼120 nm) in CTL−CQD solid, the dimer would have quenched most of the PL emissions from band-edge efficiently, indicating that the trap emission is mainly attributed to surface defects rather than dimers.

We also performed ultrafast TA measurements to track the charge-carrier detrapping kinetics. We pumped the CQD films using a sub-band gap laser pulse at 1250 nm (0.99 eV) to excite the ground- to trap-state transition and then tracked the dynamic occupation of the trap and band-edge states from 800 to 1050 nm (Figure 4d−f). We observed that the band-edge bleach feature subsequently grows within 10 ps (Figure 4d) as the intensity of the trap-state bleach feature decreases for both CTL−PbS and $PbBr_2$−PbS films. When the trap state is selectively excited, the bleach signal of band-edge is immediately observed, indicating that the trap excitation involves an electron or hole in a core band-edge level of a typical QD,[20] indicating that the trap states in the CTL−PbS films are mainly from QD surface defects, in agreement with the PL results.

We then fabricated solar cells using CTL−PbS and $PbBr_2$−PbS CQDs (Figure 5a, inset). We first investigated the thickness-dependent current density (J_{SC}) and PCE for the CTL and $PbBr_2$−PbS CQDs (Figure 5b,c). The longer L_d of the $PbBr_2$−PbS CQDs enables the fabrication of significantly thicker active layers when compared to the CTL−PbS CQDs. We obtained the best-performing $PbBr_2$−PbS devices when the active layer thickness reaches 420 nm (Figure 5a shows 470 nm of PbS film including ∼50 nm of EDT-exchanged PbS CQD film as a hole transport layer); in contrast, CTL devices show an optimized J_{SC} (∼27.5 mA cm^{-2}) and PCE (∼10.9%) at the optimal thickness of ∼370 nm, in agreement with previous reports.[7] We note that $PbBr_2$ reconstruction increases J_{SC} and optimal thickness without losing fill factor (FF) and V_{OC}. The optimal $PbBr_2$−PbS film produces a higher J_{SC} and V_{OC}, thus reaching a PCE of 12.5%.

The V_{OC}, J_{SC}, and FF of the $PbBr_2$−PbS devices are 0.64 V, 29.5 ± 1 mA cm^{-2}, and 66 ± 1%, respectively (Figure 5a). The best CTL−PbS device has a PCE as high as 10.9%, with a V_{OC}, J_{SC}, and FF at 0.62 V, 27.5 ± 1 mA cm^{-2}, and 64 ± 1%, respectively. The increased J_{SC} for $PbBr_2$−PbS films is consistent with the enhanced external quantum efficiency (EQE) in Figure 5d, with excitonic peak values of ∼80% and an integrated J_{SC} value of 29.5 mA cm^{-2} (Figure S9). We also calculated the internal quantum efficiency (IQE) using the measured EQE at 0 V bias and −2 V bias in the CQD active layer (Figure 5d), where $PbBr_2$−PbS film showed enhanced

IQE compared to that of CTL−PbS films, especially in the excitonic tail region. This enhancement agrees with the interpretation that fewer trap states and longer carrier lifetime contributes to longer carrier diffusion lengths and thus enables efficient extraction from a thicker active layer.

In conclusion, we report a CQD reconstruction to improve the PbS CQD quality to achieve high PLQY, peak-to-valley ratio, narrow HWHM, decreased dimers, and reduced surface traps, resulting in photovoltaic performance with improvements in all photovoltaic parameters (V_{OC}, J_{SC}, and FF). We mapped the density of trap states, observing a lower density of trap states, attributed to the improved surface passivation, demonstrated by the intensity-dependent PL measurements and ultrafast TA results. The resultant longer carrier lifetime is achieved by improving surface passivation and thus improved diffusion length. The CQD reconstruction improves the CQD quality, a further path to high-performance CQD solar cells and light-emitting diodes.

■ ASSOCIATED CONTENT

Supporting Information

The Supporting Information is available free of charge at https://pubs.acs.org/doi/10.1021/acs.nanolett.0c00638.

Synthesis details, methods, and additional figures (PDF)

■ AUTHOR INFORMATION

Corresponding Author

Edward H. Sargent − *Department of Electrical and Computer Engineering, University of Toronto, Toronto, Ontario M5S 3G4, Canada*; orcid.org/0000-0003-0396-6495; Email: ted.sargent@utoronto.ca

Authors

Bin Sun − *Department of Electrical and Computer Engineering, University of Toronto, Toronto, Ontario M5S 3G4, Canada*; orcid.org/0000-0002-8233-0999

Maral Vafaie − *Department of Electrical and Computer Engineering, University of Toronto, Toronto, Ontario M5S 3G4, Canada*

Larissa Levina − *Department of Electrical and Computer Engineering, University of Toronto, Toronto, Ontario M5S 3G4, Canada*

Mingyang Wei − *Department of Electrical and Computer Engineering, University of Toronto, Toronto, Ontario M5S 3G4, Canada*

Yitong Dong − *Department of Electrical and Computer Engineering, University of Toronto, Toronto, Ontario M5S 3G4, Canada*

Yajun Gao − *King Abdullah University of Science and Technology (KAUST), KAUST Solar Center (KSC), Physical Sciences and Engineering Division (PSE), Material Science and Engineering Program (MSE), Thuwal 23955-6900, Kingdom of Saudi Arabia*

Hao Ting Kung − *Department of Material Science and Engineering, University of Toronto, Toronto, Ontario M5S 3E4, Canada*

Margherita Biondi − *Department of Electrical and Computer Engineering, University of Toronto, Toronto, Ontario M5S 3G4, Canada*

Andrew H. Proppe − *Department of Electrical and Computer Engineering and Department of Chemistry, University of Toronto, Toronto, Ontario M5S 3G4, Canada*; orcid.org/0000-0003-3860-9949

Bin Chen − *Department of Electrical and Computer Engineering, University of Toronto, Toronto, Ontario M5S 3G4, Canada*

Min-Jae Choi − *Department of Electrical and Computer Engineering, University of Toronto, Toronto, Ontario M5S 3G4, Canada*

Laxmi Kishore Sagar − *Department of Electrical and Computer Engineering, University of Toronto, Toronto, Ontario M5S 3G4, Canada*; orcid.org/0000-0002-7656-7308

Oleksandr Voznyy − *Department of Electrical and Computer Engineering, University of Toronto, Toronto, Ontario M5S 3G4, Canada*; orcid.org/0000-0002-8656-5074

Shana O. Kelley − *Department of Pharmaceutical Science, Leslie Dan Faculty of Pharmacy and Department of Chemistry, University of Toronto, Toronto, Ontario M5S 3G4, Canada*; orcid.org/0000-0003-3360-5359

Frédéric Laquai − *King Abdullah University of Science and Technology (KAUST), KAUST Solar Center (KSC), Physical Sciences and Engineering Division (PSE), Material Science and Engineering Program (MSE), Thuwal 23955-6900, Kingdom of Saudi Arabia*; orcid.org/0000-0002-5887-6158

Zheng-Hong Lu − *Department of Material Science and Engineering, University of Toronto, Toronto, Ontario M5S 3E4, Canada*; orcid.org/0000-0003-2050-0822

Sjoerd Hoogland − *Department of Electrical and Computer Engineering, University of Toronto, Toronto, Ontario M5S 3G4, Canada*

F. Pelayo García de Arquer − *Department of Electrical and Computer Engineering, University of Toronto, Toronto, Ontario M5S 3G4, Canada*; orcid.org/0000-0003-2422-6234

Complete contact information is available at: https://pubs.acs.org/10.1021/acs.nanolett.0c00638

Notes

The authors declare no competing financial interest.

■ ACKNOWLEDGMENTS

This work was supported by Ontario Research Fund-Research Excellence program (ORF7 Ministry of Research and Innovation, Ontario Research Fund-Research Excellence Round 7), by the King Abdullah University of Science and Technology (KAUST) Office of Sponsored Research (OSR) under Award No. OSR-2018-CRG7-373702 and Award No. OSR-2018-CARF/CCF-3079, and by the Natural Sciences and Engineering Research Council (NSERC) of Canada. The authors acknowledge the financial support from QD Solar.

■ REFERENCES

(1) Murray, C. B.; Norris, D. J.; Bawendi, M. G. Synthesis and characterization of nearly monodisperse CdE (E = sulfur, selenium, tellurium) semiconductor nanocrystallites. *J. Am. Chem. Soc.* **1993**, *115* (19), 8706−8715.

(2) Yu, W. W.; Wang, Y. A.; Peng, X. Formation and Stability of Size-, Shape-, and Structure-Controlled CdTe Nanocrystals: Ligand Effects on Monomers and Nanocrystals. *Chem. Mater.* **2003**, *15* (22), 4300−4308.

(3) Murray, C. B.; Kagan, C. R.; Bawendi, M. G. Synthesis and characterization of monodisperse nanocrystals and close-packed nanocrystal assemblies. *Annu. Rev. Mater. Sci.* **2000**, *30*, 545−610.

(4) Sargent, E. H. Colloidal quantum dot solar cells. *Nat. Photonics* **2012**, *6* (3), 133−135.

(5) Park, Y. I.; Piao, Y.; Lee, N.; Yoo, B.; Kim, B. H.; Choi, S. H.; Hyeon, T. Transformation of hydrophobic iron oxide nanoparticles to

hydrophilic and biocompatible maghemite nanocrystals for use as highly efficient MRI contrast agent. *J. Mater. Chem.* **2011**, *21* (31), 11472−11477.

(6) Kagan, C. R.; Lifshitz, E.; Sargent, E. H.; Talapin, D. V. Building devices from colloidal quantum dots. *Science* **2016**, *353* (6302), aac5523.

(7) Liu, M.; Voznyy, O.; Sabatini, R.; Garcia de Arquer, F. P.; Munir, R.; Balawi, A. H.; Lan, X.; Fan, F.; Walters, G.; Kirmani, A. R.; Hoogland, S.; Laquai, F.; Amassian, A.; Sargent, E. H. Hybrid organic-inorganic inks flatten the energy landscape in colloidal quantum dot solids. *Nat. Mater.* **2017**, *16* (2), 258−263.

(8) Sun, B.; Voznyy, O.; Tan, H.; Stadler, P.; Liu, M.; Walters, G.; Proppe, A. H.; Liu, M.; Fan, J.; Zhuang, T.; Li, J.; Wei, M.; Xu, J.; Kim, Y.; Hoogland, S.; Sargent, E. H. Pseudohalide-Exchanged Quantum Dot Solids Achieve Record Quantum Efficiency in Infrared Photovoltaics. *Adv. Mater.* **2017**, *29* (27), 1700749.

(9) Xu, J.; Voznyy, O.; Liu, M.; Kirmani, A. R.; Walters, G.; Munir, R.; Abdelsamie, M.; Proppe, A. H.; Sarkar, A.; Garcia de Arquer, F. P.; Wei, M.; Sun, B.; Liu, M.; Ouellette, O.; Quintero-Bermudez, R.; Li, J.; Fan, J.; Quan, L.; Todorovic, P.; Tan, H.; Hoogland, S.; Kelley, S. O.; Stefik, M.; Amassian, A.; Sargent, E. H. 2D matrix engineering for homogeneous quantum dot coupling in photovoltaic solids. *Nat. Nanotechnol.* **2018**, *13* (6), 456−462.

(10) Kim, J.; Ouellette, O.; Voznyy, O.; Wei, M.; Choi, J.; Choi, M.-J.; Jo, J. W.; Baek, S.-W.; Fan, J.; Saidaminov, M. I.; Sun, B.; Li, P.; Nam, D.-H.; Hoogland, S.; Lu, Z.-H.; García de Arquer, F. P.; Sargent, E. H. Butylamine-Catalyzed Synthesis of Nanocrystal Inks Enables Efficient Infrared. *Adv. Mater.* **2018**, *30* (45), 1803830.

(11) Chuang, C.-H. M.; Brown, P. R.; Bulović, V.; Bawendi, M. G. Improved performance and stability in quantum dot solar cells through band alignment engineering. *Nat. Mater.* **2014**, *13*, 796.

(12) Choi, M. J.; Garcia de Arquer, F. P.; Proppe, A. H.; Seifitokaldani, A.; Choi, J.; Kim, J.; Baek, S. W.; Liu, M.; Sun, B.; Biondi, M.; Scheffel, B.; Walters, G.; Nam, D. H.; Jo, J. W.; Ouellette, O.; Voznyy, O.; Hoogland, S.; Kelley, S. O.; Jung, Y. S.; Sargent, E. H. Cascade surface modification of colloidal quantum dot inks enables efficient bulk homojunction photovoltaics. *Nat. Commun.* **2020**, *11* (1), 103.

(13) Chuang, C. H.; Maurano, A.; Brandt, R. E.; Hwang, G. W.; Jean, J.; Buonassisi, T.; Bulovic, V.; Bawendi, M. G. Open-circuit voltage deficit, radiative sub-bandgap states, and prospects in quantum dot solar cells. *Nano Lett.* **2015**, *15* (5), 3286−94.

(14) Zhitomirsky, D.; Kramer, I. J.; Labelle, A. J.; Fischer, A.; Debnath, R.; Pan, J.; Bakr, O. M.; Sargent, E. H. Colloidal quantum dot photovoltaics: the effect of polydispersity. *Nano Lett.* **2012**, *12* (2), 1007−12.

(15) Zhitomirsky, D.; Voznyy, O.; Levina, L.; Hoogland, S.; Kemp, K. W.; Ip, A. H.; Thon, S. M.; Sargent, E. H. Engineering colloidal quantum dot solids within and beyond the mobility-invariant regime. *Nat. Commun.* **2014**, *5*, 3803.

(16) Voznyy, O.; Levina, L.; Fan, J. Z.; Askerka, M.; Jain, A.; Choi, M.-J.; Ouellette, O.; Todorović, P.; Sagar, L. K.; Sargent, E. H. Machine Learning Accelerates Discovery of Optimal Colloidal Quantum Dot Synthesis. *ACS Nano* **2019**, *13* (10), 11122−11128.

(17) Ip, A. H.; Thon, S. M.; Hoogland, S.; Voznyy, O.; Zhitomirsky, D.; Debnath, R.; Levina, L.; Rollny, L. R.; Carey, G. H.; Fischer, A.; Kemp, K. W.; Kramer, I. J.; Ning, Z.; Labelle, A. J.; Chou, K. W.; Amassian, A.; Sargent, E. H. Hybrid passivated colloidal quantum dot solids. *Nat. Nanotechnol.* **2012**, *7* (9), 577−582.

(18) Tang, J.; Kemp, K. W.; Hoogland, S.; Jeong, K. S.; Liu, H.; Levina, L.; Furukawa, M.; Wang, X.; Debnath, R.; Cha, D.; Chou, K. W.; Fischer, A.; Amassian, A.; Asbury, J. B.; Sargent, E. H. Colloidal-quantum-dot photovoltaics using atomic-ligand passivation. *Nat. Mater.* **2011**, *10* (10), 765−771.

(19) Winslow, S. W.; Liu, Y.; Swan, J. W.; Tisdale, W. A. Quantification of a PbClx Shell on the Surface of PbS Nanocrystals. *ACS Materials Letters* **2019**, *1* (2), 209−216.

(20) Gilmore, R. H.; Liu, Y.; Shcherbakov-Wu, W.; Dahod, N. S.; Lee, E. M. Y.; Weidman, M. C.; Li, H.; Jean, J.; Bulović, V.; Willard, A. P.; Grossman, J. C.; Tisdale, W. A. Epitaxial Dimers and Auger-Assisted Detrapping in PbS Quantum Dot Solids. *Matter* **2019**, *1* (1), 250−265.

(21) Zherebetskyy, D.; Scheele, M.; Zhang, Y.; Bronstein, N.; Thompson, C.; Britt, D.; Salmeron, M.; Alivisatos, P.; Wang, L. W. Hydroxylation of the surface of PbS nanocrystals passivated with oleic acid. *Science* **2014**, *344* (6190), 1380−4.

(22) Yuan, M.; Liu, M.; Sargent, E. H. Colloidal quantum dot solids for solution-processed solar cells. *Nat. Energy* **2016**, *1*, 16016.

(23) Lan, X.; Voznyy, O.; García de Arquer, F. P.; Liu, M.; Xu, J.; Proppe, A. H.; Walters, G.; Fan, F.; Tan, H.; Liu, M.; Yang, Z.; Hoogland, S.; Sargent, E. H. 10.6% Certified Colloidal Quantum Dot Solar Cells via Solvent-Polarity-Engineered Halide Passivation. *Nano Lett.* **2016**, *16* (7), 4630−4634.

(24) Cao, Y. M.; Stavrinadis, A.; Lasanta, T.; So, D.; Konstantatos, G. The role of surface passivation for efficient and photostable PbS quantum dot solar cells. *Nat. Energy* **2016**, *1*, 16035.

(25) Wang, Y.; Lu, K.; Han, L.; Liu, Z.; Shi, G.; Fang, H.; Chen, S.; Wu, T.; Yang, F.; Gu, M.; Zhou, S.; Ling, X.; Tang, X.; Zheng, J.; Loi, M. A.; Ma, W. In Situ Passivation for Efficient PbS Quantum Dot Solar Cells by Precursor Engineering. *Adv. Mater.* **2018**, *30* (16), No. 1704871.

(26) Zhang, J.; Gao, J.; Miller, E. M.; Luther, J. M.; Beard, M. C. Diffusion-controlled synthesis of PbS and PbSe quantum dots with in situ halide passivation for quantum dot solar cells. *ACS Nano* **2014**, *8* (1), 614−22.

(27) Moreels, I.; Lambert, K.; Smeets, D.; De Muynck, D.; Nollet, T.; Martins, J. C.; Vanhaecke, F.; Vantomme, A.; Delerue, C.; Allan, G.; Hens, Z. Size-Dependent Optical Properties of Colloidal PbS Quantum Dots. *ACS Nano* **2009**, *3* (10), 3023−3030.

(28) Wang, Y.; Liu, Z.; Huo, N.; Li, F.; Gu, M.; Ling, X.; Zhang, Y.; Lu, K.; Han, L.; Fang, H.; Shulga, A. G.; Xue, Y.; Zhou, S.; Yang, F.; Tang, X.; Zheng, J.; Antonietta Loi, M.; Konstantatos, G.; Ma, W. Room-temperature direct synthesis of semi-conductive PbS nanocrystal inks for optoelectronic applications. *Nat. Commun.* **2019**, *10* (1), 5136.

(29) Shimpi, J. R.; Sidhaye, D. S.; Prasad, B. L. V. Digestive Ripening: A Fine Chemical Machining Process on the Nanoscale. *Langmuir* **2017**, *33* (38), 9491−9507.

(30) Zhang, C.; Xia, Y.; Zhang, Z.; Huang, Z.; Lian, L.; Miao, X.; Zhang, D.; Beard, M. C.; Zhang, J. Combination of Cation Exchange and Quantized Ostwald Ripening for Controlling Size Distribution of Lead Chalcogenide Quantum Dots. *Chem. Mater.* **2017**, *29* (8), 3615−3622.

(31) Razgoniaeva, N.; Yang, M.; Garrett, P.; Kholmicheva, N.; Moroz, P.; Eckard, H.; Royo Romero, L.; Porotnikov, D.; Khon, D.; Zamkov, M. Just Add Ligands: Self-Sustained Size Focusing of Colloidal Semiconductor Nanocrystals. *Chem. Mater.* **2018**, *30* (4), 1391−1398.

(32) Dagtepe, P.; Chikan, V. Quantized Ostwald Ripening of Colloidal Nanoparticles. *J. Phys. Chem. C* **2010**, *114* (39), 16263−16269.

(33) Hines, M. A.; Scholes, G. D. Colloidal PbS nanocrystals with size-tunable near-infrared emission: Observation of post-synthesis self-narrowing of the particle size distribution. *Adv. Mater.* **2003**, *15* (21), 1844−1849.

(34) Kirkwood, N.; Monchen, J. O. V.; Crisp, R. W.; Grimaldi, G.; Bergstein, H. A. C.; du Fossé, I.; van der Stam, W.; Infante, I.; Houtepen, A. J. Finding and Fixing Traps in II−VI and III−V Colloidal Quantum Dots: The Importance of Z-Type Ligand Passivation. *J. Am. Chem. Soc.* **2018**, *140* (46), 15712−15723.

(35) Seth, J.; Prasad, B. L. V. J. N. R. Bromide ion mediated modification to digestive ripening process: Preparation of ultra-small Pd, Pt, Rh and Ru nanoparticles. *Nano Res.* **2016**, *9* (7), 2007−2017.

(36) Weidman, M. C.; Beck, M. E.; Hoffman, R. S.; Prins, F.; Tisdale, W. A. Monodisperse, Air-Stable PbS Nanocrystals via Precursor Stoichiometry Control. *ACS Nano* **2014**, *8* (6), 6363−6371.

(37) Klimov, V. I.; Mikhailovsky, A. A.; McBranch, D. W.; Leatherdale, C. A.; Bawendi, M. G. Mechanisms for intraband energy relaxation in semiconductor quantum dots: The role of electron-hole interactions. *Phys. Rev. B: Condens. Matter Mater. Phys.* **2000**, *61* (20), R13349−R13352.

(38) Klimov, V. V.; Mikhailovsky, A. A.; McBranch, D. W.; Leatherdale, C. A.; Bawendi, M. G. Quantization of multiparticle auger rates in semiconductor quantum dots. *Science* **2000**, *287* (5455), 1011−3.

(39) Carey, G. H.; Levina, L.; Comin, R.; Voznyy, O.; Sargent, E. H. Record Charge Carrier Diffusion Length in Colloidal Quantum Dot Solids via Mutual Dot-To-Dot Surface Passivation. *Adv. Mater.* **2015**, *27* (21), 3325−30.

(40) Proppe, A. H.; Xu, J.; Sabatini, R. P.; Fan, J. Z.; Sun, B.; Hoogland, S.; Kelley, S. O.; Voznyy, O.; Sargent, E. H. Picosecond Charge Transfer and Long Carrier Diffusion Lengths in Colloidal Quantum Dot Solids. *Nano Lett.* **2018**, *18* (11), 7052−7059.

(41) Dong, Q.; Fang, Y.; Shao, Y.; Mulligan, P.; Qiu, J.; Cao, L.; Huang, J. Electron-hole diffusion lengths > 175 μm in solution-grown $CH_3NH_3PbI_3$ single crystals. *Science* **2015**, *347* (6225), 967−970.

(42) Stadler, P.; Sutherland, B. R.; Ren, Y.; Ning, Z.; Simchi, A.; Thon, S. M.; Hoogland, S.; Sargent, E. H. Joint Mapping of Mobility and Trap Density in Colloidal Quantum Dot Solids. *ACS Nano* **2013**, *7* (7), 5757−5762.

(43) Oh, S. J.; Straus, D. B.; Zhao, T.; Choi, J. H.; Lee, S. W.; Gaulding, E. A.; Murray, C. B.; Kagan, C. R. Engineering the surface chemistry of lead chalcogenide nanocrystal solids to enhance carrier mobility and lifetime in optoelectronic devices. *Chem. Commun.* **2017**, *53* (4), 728−731.

(44) Schmidt, T.; Lischka, K.; Zulehner, W. Excitation-power dependence of the near-band-edge photoluminescence of semiconductors. *Phys. Rev. B: Condens. Matter Mater. Phys.* **1992**, *45* (16), 8989−8994.

https://dx.doi.org/10.1021/acs.nanolett.0c00638